HHS Public Access

Author manuscript

Biomaterials. Author manuscript; available in PMC 2019 April 28.

Published in final edited form as:

Biomaterials. 2018 December ; 185: 348–359. doi:10.1016/j.biomaterials.2018.09.015.

Spatially controlled assembly of affinity ligand and enzyme cargo enables targeting ferritin nanocarriers to caveolae

Vladimir V. Shuvaev[a], **Makan Khoshnejad**[a], **Katherine W. Pulsipher**[b], **Raisa Yu. Kiseleva**[a], **Evguenia Arguiri**[c], **Jasmina C. Cheung-Lau**[b], **Kathleen M. LeFort**[a], **Melpo Christofidou-Solomidou**[c], **Radu V. Stan**[d], **Ivan J. Dmochowski**[b], and **Vladimir R. Muzykantov**[a,*]

[a]Department of Pharmacology and Center for Translational Targeted Therapeutics and Nanomedicine of the Institute for Translational Medicine and Therapeutics, University of Pennsylvania, Philadelphia, PA, United States

[b]Department of Chemistry, University of Pennsylvania, Philadelphia, PA, United States

[c]Department of Medicine, Pulmonary, Allergy and Critical Care Division, University of Pennsylvania, Philadelphia, PA, United States

[d]Department of Biochemistry and Cell Biology, Geisel School of Medicine at Dartmouth, Lebanon, NH, United States

Abstract

One of the goals of nanomedicine is targeted delivery of therapeutic enzymes to the sub-cellular compartments where their action is needed. Endothelial caveolae-derived endosomes represent an important yet challenging destination for targeting, in part due to smaller size of the entry aperture of caveolae (ca. 30–50 nm). Here, we designed modular, multi-molecular, ferritin-based nanocarriers with uniform size (20 nm diameter) for easy drug-loading and targeted delivery of enzymatic cargo to these specific vesicles. These nanocarriers targeted to caveolar Plasmalemmal Vesicle-Associated Protein (Plvap) deliver superoxide dismutase (SOD) into endosomes in endothelial cells, the specific site of influx of superoxide mediating by such pro-inflammatory signaling as some cytokines and lipopolysaccharide (LPS). Cell studies showed efficient internalization of Plvap-targeted SOD-loaded nanocarriers followed by dissociation from caveolin-containing vesicles and intracellular transport to endosomes. The nanocarriers had a profound protective anti-inflammatory effect in an animal model of LPS-induced inflammation, in agreement with the characteristics of their endothelial uptake and intracellular transport, indicating that these novel, targeted nanocarriers provide an advantageous platform for caveolae-dependent delivery of biotherapeutics.

Keywords

Ferritin nanocage; Protein nanoparticle; Superoxide dismutase; Endothelial targeting; Inflammation

*Corresponding author. muzykant@pennmedicine.upenn.edu (V.R. Muzykantov).

Appendix A. Supplementary data

Supplementary data related to this article can be found at https://doi.org/10.1016/j.biomaterials.2018.09.015.

1. Introduction

Nanocarrier structure, payload, targeting and other elements must be assembled in a mutually agreeable way [1–3]. Targets with limited access represent a special case in this context. On the one hand, carrier miniaturization helps enable an access to such targets. On the other hand, the smaller the carrier, the more challenging to attain needed payload and configure carrier's elements in a spatially optimal fashion on nanometer scale [4].

Caveolae are flask-shaped invaginations formed in cholesterol-rich domains of the plasma membrane, decorated on the cytosolic side by the caveolins, cavins and other proteins [5]. They are found in diverse cell types and are especially abundant in the pulmonary endothelium [6,7]. Caveolae exert transporting and regulatory functions [8] and represent an important, intriguing target for drug delivery [9–12] in conditions including inflammation and tumors [13].

Plasmalemmal Vesicle-Associated Protein (Plvap/PVl) is an endothelial glycoprotein involved in control of vascular permeability, leukocyte traffic and other functions [14]. In the lungs and kidneys it localizes predominantly in caveolae and endothelial fenestrae, respectively [15,16].

Antibodies and other ligands of caveolar determinants including Plvap are being explored for endothelial drug targeting [17]. They accumulate in the lungs after intravascular injection [9,11,17,18]. However, caveolae represent a classical example of a target with limited access [19]. The internal diameter of caveolae stomata aperture is considered to be less than 30 nm [15]. Nanoparticles of larger size coated by the caveolar ligands are therefore unable to access Plvap [18].

Ferritins are a family of proteins responsible for the oxidation and storage of iron in all kingdoms of life [20]. The ferritin oligomeric complex consists of two dozen paired alpha-helical bundle monomers, which, depending on pH, ionic strength and other conditions reversibly assemble into a symmetrical hollow particle with mean diameter of 10–12 nm, interior cavity of 8nm and narrow size distribution [20]. These features, as well as amenability to chemical and recombinant modification, make the ferritin oligomeric complexes potentially versatile carrier platforms for diverse drug delivery and imaging purposes [21,22]. The size of ferritin particles may also provide advantages in targeting to sites with limited accessibility including caveolae. Here, we utilized thermophilic ferritin that exists in reversible disassembled state in low salt conditions and assembles into the molecular cage in high salt [23] allowing easy loading of sensitive drugs such as biotherapeutics (i.e. enzymes) in physiological conditions without affecting their catalytic or other properties.

Lipopolysaccharide (LPS) and some cytokines [24] bind to receptors in the cholesterol-rich domains of cell membrane, internalize via caveolar endocytosis and ignite an influx of superoxide in endosomal lumen [25], leading to pathological activation of cells [26,27]. Targeting superoxide dismutase (SOD) to caveolae may intercept this pathway [28], providing anti-inflammatory effects [25,29].

Here we designed ferritin nanocarriers assembled to carry both Plvap antibody and SOD in a distinct, spatially controlled manner and studied their targeting, cellular localization and therapeutic activity.

2. Materials and methods

2.1. Reagents and antibodies

Dimethylformamide (DMF), dimethyl sulfoxide (DMSO), fetal bovine serum, lipopolysaccharide (LPS) from *E. coli* 055:B5, and ferritin form horse spleen were purchased from Sigma (St. Louis, MO). Cu, Zn-SOD from bovine erythrocytes (dimer, 32.5 kDa) is from Calbiochem (San Diego, CA), 4-[*N*-maleimidomethyl] cyclohexane-1-carboxylate (SMCC), N-succinimidyl-S-acetylthioacetate (SATA) were from ThermoFisher Scientific (Grand Island, NY). Monoclonal antibody MEC13.3 towards murine Platelet endothelial cell adhesion molecule (PECAM) was from BD Biosciences (San Jose, CA). MECA32 hybridoma was obtained from the Developmental Studies Hybridoma Bank (developed under the auspices of the NICHD and maintained at the University of Iowa, Department of Biology, Iowa City, IA 52242). Cells were grown in serum-free PFHM-2 and antibody to murine PV1/PLVAP was purified using Protein G-Sepharose 4 Fast flow. For Western blot analysis (WB) and immunocytochemistry (ICC) the following antibodies were used: goat polyclonal anti-mouse vascular cell adhesion molecule-1 (VCAM-1) and anti-mouse PECAM-1 (Santa-Cruz Biotech., Dallas, TX), anti-beta-actin, conjugated to HRP, rabbit polyclonal anti-EEA-1 (Cell Signaling), rabbit monoclonal anti-caveolin-1, anti-LAMP-2α, anti-giantin, anti-interleukin 1 beta (Abcam, Cambridge, MA). The secondary antibodies, anti-goat-HRP were from Santa-Cruz, whereas chicken anti-rabbit Alexa Fluor 488 labeled, goat anti-rat Alexa Fluor 488 or 594 labeled were from Invitrogen (ThermoFisher Scientific), chicken anti-goat Alexa Fluor 647 labeled were from Life Technologies Molecular Probes (ThermoFisher Scientific).

2.2. Thermophilic ferritin expression and purification

Wild type (WT) thermophilic ferritin (tF) from 522 base pairs (bp) *Archaeoglobus fulgidus* gene AF 0834 (i.e. tF) was expressed and purified as previously published, with minor modifications [23,30]. The assembled ferritin nanocage is characterized by relatively large (4.5 nm) pores and an 8-nm diameter internal cavity [30,31]. The plasmid coding for WT tF was purchased from DNA 2.0. The plasmid coding for cysteine-containing tF1iC (mutation E131C) was generated using the Quik Change site-directed mutagenesis kit (Stratagene/Agilent) using the following primers purchased from Integrated DNA Technologies:

forward (5′-3′): GTACGTTGCTGAACAAGTGTGCGAGGAAGCGAGCGCCCTG.

reverse (5′-3′): CAGGGCGCTCGCTTCCTCGCACACTTGTTCAGCAACGTAC.

Plasmids were transformed into *E. coli* BL21-CodonPlus(DE3)-RP cells and cultured overnight with shaking at 30 °C in Luria-Bertani medium, supplemented with 100 μg/mL ampicillin and 35 μg/mL chloramphenicol. Cultures were then transferred to 1 L Terrific Broth supplemented with 100 μg/mL ampicillin and 35 μ/mL chloramphenicol and grown

with shaking at 37 °C until OD_{600} ~0.8. Expression was induced with 1 mM isopropyl β-D-1-thiogalactopyranoside (IPTG) for 4 h with shaking at 37 °C.

Cell lysis was done via treatment with lysozyme for 30 min at room temperature, followed by sonication. Cellular debris were removed by centrifugation (30 min, 6 krpm, 4 °C). The resulting supernatant was treated with DNase for 15 min at room temperature, followed by heat shocking for 10 min at 80 °C. Precipitated proteins were removed by centrifugation (60 min, 9 krpm, 4 °C). The supernatant containing tF or tF1iC was concentrated, buffer exchanged (20 mM sodium phosphate, 2.5 M NaCl, 2 mM EDTA, pH 7.6), and filtered with a 0.22 μm syringe filter. Final purification was done via size exclusion chromatography, using a HiLoad 16/60 column connected to an AKTA FPLC and equilibrated with 20 mM sodium phosphate, 800 mM NaCl, pH 7.6. Concentration was determined by Bradford assay, using bovine gamma globulin as a standard. SDS-electrophoresis of both WT tF and tF1iC showed the major protein band of expected sizes of 21–22 kDa (Suppl. Fig. S3). Protein purity was estimated to be >95%. Multiple protein preparations were used for the experiments presented below.

2.3. SOD iodination, labeling with fluorophore, and activity

In some experiments SOD was either fluorescently labeled with Alexa Fluor 488 or iodinated with ^{125}I before conjugation to tF1iC. Alexa Fluor 488 NHS ester (Molecular Probes, ThermoFisher) was used to fluorescently label SOD. AF488-SOD was used for confirmation of introducing SOD inside thermophilic ferritin particles. For *in vivo* biodistribution studies the enzyme was radiolabeled with $Na^{125}I$ (PerkinElmer) using Pierce Iodination Beads (Thermo Scientific, Rockford, IL) as recommended by the manufacturer. Free I was removed by Zeba Micro Spin Desalting Columns (Thermo, Rockford, IL). SOD catalytic activity was measured by cytochrome c assay [32].

2.4. Two approaches for preparation of multimolecular ferritin conjugates with antibodies and SOD

We have pursued two principal approaches, described in detail below. In the first approach, antibody and SOD were conjugated to the external surface of mammalian Ft from horse spleen, producing (Ab + SOD)/Ft. In the second approach SOD was encapsulated in the inner cavity of the mutant form of tF, containing a single cysteine residue per subunit facing towards the inside of the cavity of the assembled ferritin nanocage (tF1iC). This conjugate was designated Ab/(Ft/SOD).

2.4.1. Mammalian ferritin conjugation to enzyme drug and antibody—

Heterobifunctional crosslinkers SATA and SMCC were used for conjugation of antibody and SOD to horse spleen Ft as described earlier [33]. SATA was added at 1:5 M ratio of antibody or SOD to SATA for 30 min at rt. SATA was then de-protected using 10% 0.5 M hydroxylamine for 2 h at room temperature. Ft was added at 1:150 M ratio of Ft (based on Ft 24-mer molar concentration) to SMCC for introducing maleimide groups. Antibody and SOD conjugation to Ft was carried out at 1:10 M ratio of Ft to mixture of antibody and SOD for 1 h at room temperature. Unbound reagents were removed by desalting columns. The nanocarriers were purified by size-exclusion high-performance liquid chromatography

(SEC-HPLC) using BioSep SEC-s3000 column (Phenomenex, Torrance, CA). The samples were purified by isocratic method with PBS pH 7.4 to remove free antibody [33]. For experiments with drug-free ferritin nanocages, antibodies were conjugated to ferritin in the absence of SOD.

2.4.2. Thermophilic ferritin drug-loading—Preparation of thermophilic ferritin containing single inward-looking cysteine tF1iC loaded with SOD and conjugated with appropriate antibody for targeting was performed in three steps (Fig. 1). First, tF1iC was transferred from high salt (1 M NaCl) to phosphate-buffered saline (PBS, 0.15 M NaCl). tF1iC (10mg/mL) was reduced in the presence of 20 mM freshly prepared TCEP (tris(2-carboxyethyl)phosphine), 0.5mM EDTA, pH 7.5 for 1 h at room temperature. SOD (94 μM) was modified by SMCC at molar ratio SOD:SMCC 1:12 also for 1 h at room temperature. Unreacted reagents were removed from both proteins by desalting columns. Then reduced tF1iC and maleimide-SOD were mixed at molar ratio tF:SOD 2:1 (considering molar concentration of tF monomer) and conjugation was performed for 1 h at room temperature. The mixture was then transferred to 1 M NaCl/PBS to allow the assembly of the tF nanocage. Unbound SOD was removed using FPLC (see detailed FPLC description below) and tF1iC/SOD was concentrated to approximately 1–1.2 mg/mL of protein as assayed by the Lowry method.

2.4.3. Thermophilic ferritin crosslinking—In the second step tF1iC was crosslinked to preserve nanocage configuration and to prevent tF disassembling upon its transfer to PBS. Crosslinking was performed using $BS(PEG)_5$ (bis-N-succinimidyl-(pentaethylene glycol)) ester (Thermo). Optimal conditions for effective cross-linking were confirmed in preliminary experiments. Purified and concentrated tF1iC was transferred into 1 M NaCl/50 mM HEPES, pH and $BS(PEG)_5$ was added at molar ratio tF:crosslinker 1:5 for 30 min at room temperature. Crosslinked tF1iC/SOD was separated from unreacted crosslinker and transferred into PBS.

2.4.4. Conjugation of thermophilic ferritin to antibody—As a final step of antibody-tF1iC conjugate preparation antibodies were conjugated to cross-linked tF1iC/SOD using amino-based chemistry described earlier [29]. Maleimide groups were introduced into tF using SMCC at a molar ratio tF:SMCC 1:12, while protected sulfhydryl groups were introduced in antibody molecules by SATA at a molar ratio Ab:SATA 1:6. After deprotection of sulfhydryl groups on the antibody the conjugation reaction between tF and antibody (Ab) was performed at equimolar Ab:tF (one IgG per tF monomer) ratio for 1 h at room temperature. Unreacted antibodies were removed by FPLC as described below. Final preparation of Ab/tF1iC/SOD was characterized by SDS-electrophoresis in Tris-glycine (for middle-sized proteins; Mini-Protean TGX gel, 4–15%, Bio-Rad) or Tris-acetate (for large protein assemblies; NuPAGE 3–8%, Invitrogen) systems as well as dynamic light scattering (DLS), transmission electron microscopy (TEM), and cytochrome c assay for SOD activity. In some experiments SOD was labeled with Alexa Fluor 488 or iodinated with ^{125}I before conjugation to tF1iC. For experiments with drug-free Ft nanocages antibodies were conjugated to crosslinked WT ferritin without preliminary SOD loading.

2.4.5. Analytical size exclusion chromatography and fluorescence measurements—

Samples of tF1iC-SOD labeled with Alexa Fluor 488 were analyzed on a Superdex200 10/300 GL column equilibrated with 1 M NaCl PBS and connected to an AKTA FPLC. Samples were analyzed at 4 °C in the dark, with a flow rate of 0.5mL/min. Fractions were collected and analyzed by steady-state fluorescence using a Varian Cary Eclipse fluorescence spectrophotometer using a 100 μL quartz cuvette. The excitation wavelength used was 496 nm, with a scan rate of 30 nm/min, and a PMT voltage of 600 or 800 V, depending on the sample concentration.

2.5. Transmission electron microscopy

Ft particles were applied on a TEM grid (Formvar Film 200 mesh; Electron Microscopy Sciences, Hartfield, PA) followed by negative staining with 2% (w/v) uranyl acetate. Images were taken using JEM-1010 Transmission Electron Microscope (JEOL USA, Inc., Peabody, MA). Magnification of 200,000x was used for particle visualization.

2.6. Dynamic light scattering

The effective diameter of the prepared particles was measured by DLS using a Zetasizer Nano ZSP (Malvern Instruments Ltd., Malvern, UK). The measurements were done at 25 °C using 2 min as an equilibration time.

2.7. SDS-polyacrylamide gel electrophoresis and Western blotting

Lung tissue was homogenized in PBS supplemented with protease inhibitor cocktail using a TissueLyser II (Qiagen, Valencia, CA) with 5-mm stainless steel bead for 6 min at 30 Hz. Next, cells were lysed after addition of lysis buffer (0.5% Triton X-100, 0.5% SDS, final concentrations) for 1 h at 4 °C while slow rotating. Samples were sonicated with Sonic Dismembrator 60 (Fisher) and centrifuged at 16,000x*g* for 10 min. Total protein concentration was measured in the supernatant by the Lowry assay. Samples were mixed with sample buffer for SDS-polyacrylamide gel electrophoresis (SDS-PAGE) and then were subjected to 4–15% gradient SDS-electrophoresis. Gels were transferred to PVDF membrane (Millipore), and the membrane was blocked with 3% nonfat dry milk in TBST (100 mM Tris (pH 7.5), 150 mM NaCl, 0.1% Tween 20) for 1 h followed by incubations with primary and secondary antibodies in the blocking solution. The blot was detected using ECL Plus reagents (GE Healthcare).

2.8. Cell experiments

2.8.1. Cell culture—

Murine endothelial cells bEnd3 were obtained from ATCC (Manassas, VA) and were grown in DMEM with 10% fetal bovine serum and antibiotic/antimycotic. For microscopic studies bEnd3 cells were grown on microscope 12-mm glass coverslips, treated with 1% gelatin.

2.8.2. Cell internalization studies—

For internalization studies bEnd3 cells were treated with Plvap-directed Ab/(Ft/SOD) at 37 °C in complete medium for indicated time. Cells were stained as described [34]. Briefly, cells were washed three times with PBS, and fixed with ice-cold 2% paraformaldehyde for 15 min at rt. First, cells were incubated with

Alexa Fluor 594-labeled goat anti-rat IgG (MECA32 clone is a rat IgG2a monoclonal antibody) (reference) for 1 h at rt. Unbound antibodies were washed, and cells were permeabilized with 0.2% Triton X-100 for 15 min. Next permeabilized cells were stained with Alexa Fluor 488 goat anti-rat IgG for 1 h at room temperature. Samples were washed and mounted using ProLong Gold antifade reagent with DAPI (Invitrogen). Fluorescence images (slices of 0.3 μm) were acquired using a confocal laser scanning microscope Leica TCS-SP8 (Leica, Germany) using HC PL APO CS2 63x/1.40 Oil objective and 488/552/638 lasers. Single-labeled conjugates (appeared as green) were considered as internalized while double-labeled conjugates (appeared as yellow) were considered to be extracellular. Microscope control and image processing were carried out using Image-Pro Plus 4.5.1.27 (Media Cybernetics, Bethesda, MD, USA) as described earlier [35]. Whole cell reconstructed 3D images were split using ImageJ. Each slice was analyzed separately, and the internalization rate was summarized and calculated for each field. At least three fields for each condition were analyzed. Internalization rate was calculated as ratio of voxels that have both particle signal and organelle marker to total particle-containing voxels and expressed as % internalization. Internalization rate was normalized to initial time (t = 0). Kinetics were analyzed by GraphPad Prism software (La Jolla, CA) using binding kinetics with ‘one phase exponential decay’ model.

2.8.3. Intracellular co-localization studies—Cells were grown on 1% gelatin-coated glass coverslips. After incubation with Ft nanocages, cells were washed, fixed with ice-cold 2% paraformaldehyde for 15 min and permeabilized with 0.2% Triton X-100 for 15 min prior to staining with antibodies. Conjugates were stained with Alexa Fluor 594-labeled goat anti-rat IgG. Rabbit antibodies to caveolin-1, EEA1, LAMP-2α, or giantin were used to stain caveolae, endosomes, lysosomes, or Golgi apparatus, respectively. After washing cells were visualized by Alexa Fluor 488-labeled chicken anti-rabbit secondary antibodies. Finally, samples were mounted using ProLong Gold Antifade Reagent with DAPI (Molecular Probes, ThermoFisher). In case of triple staining of Plvap, PECAM, and giantin in addition to rat anti-Plvap and rabbit anti-giantin antibodies we used goat polyclonal antibody to PECAM followed by Alexa Fluor 647-labeled chicken anti-goat secondary antibody. Co-localization studies were performed on a confocal laser scanning microscope Leica TCS-SP8 (Leica, Germany) using HC PL APO CS2 63x/1.40 Oil objective and 488/552/638 lasers. Images were processed and Manders’ Overlap Coefficient (MOC) [36] was calculated using Volocity 6.3 Cellular Imaging & Analysis.

2.9. Biodistribution of antibody-ferritin particles in vivo

Animal experiments were performed according to the protocol approved by the Institutional Animal Care and Use Committee (IACUC) of the University of Pennsylvania. I^{125}-SOD (10mol%) was used to prepare I^{125}-labeled Ab-Ft-SOD nanoparticles and were injected IV (10 μg of SOD) in normal C-57BL/65 mice (The Jackson Laboratory, Bar Harbor, ME) via tail vein. After 1 h, the internal organs were harvested, rinsed with saline, blotted dry, and weighed. Tissue radioactivity in organs and 100-μl samples of blood was determined in a Wallac 1470 Wizard™ gamma counter. The percentage of injected dose in an organ (%ID) measures the total amount of Ab uptake in an organ, showing biodistribution and effectiveness of Ab uptake.

2.10. Endotoxemia model in mice

The set of *in vivo* experiments was conducted in accordance with the guidelines approved by the Institutional Animal Care and Use Committee at University of Pennsylvania and was performed on 6–8-week-old male C57BL/6 mice (20–25 g). Ab/SOD conjugates were injected 15 min prior LPS (2.0 μg/kg) via tail vein [29]. 5 h after LPS challenge lungs were perfused with PBS and harvested. VCAM-1 expression was analyzed by Western blot.

2.11. Statistical analyses

All values were expressed as means ± SD. For comparison of two groups, statistical significance was estimated by Student's *t*-test, where $P \leq 0.05$ was considered significant.

3. Results

3.1. Molecular design and features of two configurations of ferritin nanocarriers conjugated with antibody and SOD: (Ab + SOD)/Ft and Ab/(Ft/SOD)

We designed two types of tri-molecular conjugates of ferritin with an affinity ligand (anti-Pvlap antibody, Ab, or appropriate control IgG) and enzyme cargo (SOD).

In the first iteration, designated as (Ab + SOD)/Ft, both SOD and Ab were conjugated to the outer surface of Ft particles (Suppl. Fig. S1). This did not change appearance in TEM of negatively stained Ft nanoparticles typical of mammalian Ft assembly [33] (Suppl. Fig. S1, a-e). DLS showed that the size of Ab/(Ft + SOD) was ~ 25 nm, whereas the size of intact Ft particle was ~ 12 nm (Suppl. Fig. S1, f-h).

In the second iteration, designated as Ab/(Ft/SOD), Ab and SOD were selectively conjugated to the outer and inner surface of the Ft particle, respectively. To achieve this, we used a mutant form tF1iC. This enables site-specific conjugation of cargo inside the Ft nanocage. Assembly and disassembly of tF is controlled by ionic strength [37], which enables facile encapsulation of useful enzyme cargo within the protein interior in physiological conditions [31,38,39].

This approach yields a formulation with spatially distinct localization of Ab and SOD at the outer and inner surfaces of the particles, respectively. Conjugation of fluorescently labeled SOD (AF488-SOD) to tF1iC was confirmed by SDS-PAGE (Fig. 2A), FPLC (Fig. 2B), and spectroscopic analysis (Fig. 2C and D). SDS-PAGE confirmed that maleimide-SOD (15 kDa band) and reduced ferritin (22 kDa band) formed conjugates (major 35 and minor 50 kDa bands). FPLC allowed clear separation of 450-kDa Ft nanocages and 31-kDa unbound SOD (Fig. 2B). It's of note that tF1iC/SOD nanocage run the same way as original tF1iC nanocage indicating that SOD conjugation does not change the overall size of Ft particles that was also confirmed by DLS analysis.

Following fluorescence measurements of both peaks (Fig. 2C and D) it was confirmed that Ft peak did contain AF488-SOD (i.e. tF1iC/SOD). The yield of the SOD-ferritin conjugation was estimated ca. 2.2 SOD molecules per 24-mer ferritin nanocage based on the level of the labeled SOD in tF1iC/SOD peak. Obtained tF1iC/SOD conjugates were in disassembled state at low salt (Fig. 3A), yet assembled in 24-mer particles at high-salt buffer (Fig. 3B).

Crosslinking the particles using $BS(PEG)_5$ was performed to stabilize their structure at both high (Fig. 3C) and low ionic strength (Fig. 3D). Moreover, SDS-PAGE shows that the complex was stable even in denaturing conditions (Fig. 3E). The size of the particles was about 15nm (Fig. 4B).

Crosslinked tF1iC/SOD was further used for nanocarriers coated with anti-PLVAP or rat IgG2a isotype control. Conjugation was performed at IgG:Ft monomer equimolar ratio (i.e. 24 IgG per crosslinked nanocage) and confirmed by 3–8% gradient NuPAGE in Tris-acetate non-reduced gel electrophoresis (Fig. 4A). Unconjugated antibodies were removed by FPLC and the resulting purified Ab/(Ft/SOD) was measured by DLS, showing a size of ~ 20 nm (Fig. 4C). Therefore, both Ab/(Ft/SOD) and (Ab + SOD)/Ft displayed similar size characteristics of 20–25 nm in diameter with PDI 0.20–0.24. Earlier we have demonstrated that on average three molecules of IgG can be conjugated to the surface of Ft particle under the described conditions [40]. Therefore, one Ab/(Ft/SOD) particle contains on average 3 and 2 molecules of IgG and SOD, respectively.

3.2. Cellular uptake of Plvap-targeted conjugates

To study uptake and traffic of Plvap-targeted Ab/Ft/SOD conjugates, mouse endothelial cells bEnd3 were incubated for 2 h on ice with Ab/(Ft/SOD) in complete medium, washed, incubated at 37 °C, washed, fixed and stained to distinguish surface-bound vs. internalized particles. Fig. 5 shows that Ab(Ft/SOD) bound to the cell surface on ice was rapidly internalized at 37 °C. Binding kinetics was fitted as one phase exponential decay and corresponded to the following equation: $Y = (-5.063\text{-}89.45)*\exp(-0.07727*X) + 89.45$ ($R^2 = 0.812$) (Fig. 5B).

Further, we studied cellular localization of nanoparticles. First, we looked at relative co-localization of Plvap-targeted nanoparticles with caveolar marker. In pulse-chase setting, the majority of Ab(Ft/SOD) transiently at early time points coincided with caveolin-1, a marker of endothelial caveolae (Fig. 6). Image analysis of co-localization using Manders' overlap coefficient (MOC) showed that the double-label yellow signal attained a maximum around 10–15 min after initiation of endocytosis and markedly declined at 1 h (Fig. 6B).

3.3. Intracellular localization of Plvap-directed Ab/(Ft/SOD) nanocarriers

The data shown above suggested that Plvap-targeted Ab/(Ft/SOD) enter target cells after binding to caveolin-positive domains of the plasma. To determine the destination for the nanoparticles we visualized cells 1 h post-endocytosis initiation in pulse-chase experiments and attributed the particle colocalization with caveolae, endosomes, lysosomes, and Golgi apparatus, based on co-staining of nanoparticles and organelles using antibodies to the corresponding markers (i.e. caveolin-1, EEA-1, LAMP2, and giantin, respectively).

Analysis of confocal images included the calculation of Manders' Overlap Coefficient (MOC) that quantifies the relative degree of colocalization between two fluorophores [36]. Nanoparticles were mostly found in endosomes and lysosomes, while MOC of particles colocalization with caveolin-1-positive vesicles and Golgi apparatus were much lower (Fig. 7).

Similar to colocalization studies shown on Fig. 7 we tested 3D colocalization of Plvap-directed Ab/(Ft/SOD) with cellular markers of caveolae, endosomes, lysosomes, and Golgi at the 1 h time point that corresponds to sizeable accumulation of particles in destination organelles. Supplemental material contains videos that demonstrate co-localization of ferritin nanoparticles with caveolin-1 (Suppl. Video S1), EEA-1 (Suppl. Video S2), LAMP-2α (Suppl. Video S3), and giantin (Suppl. Video S4). Videos were based on 3D reconstruction and show Ft nanocages in red, organelles in green and nuclei in blue. In all videos, Ab/(Ft/SOD) were observed as mostly vesicular structures that can be seen in the perinuclear area in the midst of cells beneath the apical surface. The videos also demonstrate intercellular heterogeneity of the distribution of nanocarriers and compartments of interest. In line with dynamic nature of caveolae, caveolin staining appeared to have both vesicular and surface character, especially profound on the cell periphery. In agreement with previous analysis, Ft nanoparticles were often found in endosomes and lysosomes, but not with caveolin-1 or in Golgi apparatus.

We compared kinetics of trafficking in the implicated compartments. In contrast with rapid transient co-localization with caveolar compartment that declined by 1 h (Fig. 6), endosomal and lysosomal compartments showed enhanced MOC indicating co-localization increased with time and reached a plateau at 1 h (Fig. 8).

3.4. Pulmonary uptake of Plvap-targeted nanoparticles after vascular administration

In accordance with the known abundance of caveolae in the pulmonary endothelium [15,41–43], Plvap Ab, but not control IgG accumulated in the lungs (Fig. 9). Pulmonary targeting of Plvap Ab-carrying polystyrene particles with diameter 200 nm exceeding the diameter of caveolar aperture was obliterated.

In contrast, both types of drugless (i.e., lacking SOD) Plvap Ab-carrying Ft nanoparticles based on either mammalian or thermophilic Ft accumulated in lungs to an extent of 75–80 %ID/g (Fig. 9), therefore showing orders of magnitude higher targeting than IgG/Ft. This result is consistent with the notion that the target in the endothelial caveolae is effectively accessible for Ab/Ft nanoparticles with size 20–25 nm. One hour after injection, the blood level of Ab/Ft and IgG/Ft nanocarriers was 1.1 ± 0.1 and 1.2 ± 0.1%ID/g, respectively, whereas the lung level was 77.8 ± 11.2 and 3.1 ± 0.9 %ID/g, respectively (Fig. 10A). These data indicate that the lung targeting is specific and the contribution of residual blood is negligible.

3.5. Endothelial targeting of (Ab + SOD)/Ft and Ab/(Ft/SOD) in vivo

Having verified effective pulmonary targeting of drugless Plvap Ab/Ft particles, we compared their iterations containing ^{125}I-SOD conjugated to either the inner or outer Ft surface (Fig. 10, panels A and B respectively). This experiment revealed that concomitant conjugation of Ab and SOD to the outer surface of Ft particles inhibits targeting, proportionally to drug load on the Ft surface (Fig. 10B).

In contrast, SOD conjugation to the inner surface of the Ft particle did not impede targeting: parameters of the pulmonary uptake of Plvap-targeted Ab/(Ft) vs. Ab/(Ft/SOD) were nearly identical (Fig. 10A). The Immunospecificity Index (Localization Ratio of Ab-conjugated

formulation divided by IgG-conjugated counterpart [44]) of pulmonary uptake of both Ab/Ft and Ab/(Ft/SOD) conjugates was about 25.

SOD conjugation to the outer surface of the ferritin particle may competitively inhibit ligand conjugation. Our conjugation method yields Ft particles carrying ~ 4–5 full-length molecules of IgG or ~ 7–8 molecules of scFv (single chain antibody Fv-fragments) [33]. In addition, enzyme cargo molecules may impose spatial hindrance of the freedom of interaction of ligand molecules with target determinant, reducing avidity and valence of the carriers [45].

3.6. SOD surface loading inhibits endothelial targeting of Ab/Ft directed to cell adhesion molecules

In theory, inhibitory effects of conjugation of the enzymatic cargo with affinity ligand on nanocarrier surface may be especially deteriorating in case of targets with limited accessibility, such as Plvap in the caveolae. To test whether this effect is specific for such targets, we studied the pulmonary targeting of (Ab + SOD)/Ft conjugates directed to distinct endothelial determinants, intercellular cell adhesion molecules-1 and PECAM-1, that localize in the luminal plasma membrane and intercellular junctions, respectively. Accordingly, we produced (Ab + SOD)/Ft particles of similar size containing antibodies to Plvap, PECAM-1 and ICAM-1, as well as control IgG (Supplemental Fig. S2, f-h).

Both Ab/Ft and scFv/Ft conjugates bind to cells transfected with corresponding ICAM-1 or PECAM-1 antigens, but not to wild type (Fig. 11), and conjugation of SOD to the exterior surface of Ft particles yielding tri-molecular (Ab + SOD)/Ft inhibited targeting to PECAM and ICAM expressing cells mediated by either full-length antibody or scFv (Fig. 11A and B). Furthermore, pulmonary targeting of an ICAM-directed tri-molecular (Ab + SOD)/Ft conjugate was markedly inhibited in comparison to the drugless Ab/Ft (Fig. 11C). Therefore, inhibition of Ab/Ft targeting caused by co-conjugated enzyme cargo is a general phenomenon, not limited to the caveolar targets.

3.7. Comparing the anti-inflammatory effects of (Ab + SOD)/Ft vs. Ab/(Ft/SOD) in a mouse model of endotoxemia

To test functionality of the Plvap-directed targeting of tri-molecular Ab-SOD-Ft conjugates, we employed a mouse model of acute aseptic vascular inflammation induced by systemic injection of LPS [25,29]. This model is relevant to the severe conditions of endotoxemia and sepsis in human patients.

As in previous studies [25,29], LPS caused pro-inflammatory changes in the lungs, manifested by expression of the endothelium-specific cell adhesion molecule VCAM-1, marker of vascular inflammation. Furthermore, in good agreement with targeting data shown in Fig. 7, Ab/(Ft/SOD), but not (Ab + SOD)/Ft, efficiently inhibited LPS-induced pulmonary inflammation, which was evident by abrogation of level of expression of VCAM-1 (Fig. 12). Based on Ab/(Ft/ SOD) biodistribution data, injection of 75 μg of SOD in mouse delivers approximately 8.8 μg of SOD to the lungs. This amount, however, drops significantly for (Ab + SOD)/Ft nanoparticles (see Fig. 10). To test if Plvap-directed delivery of SOD affects systemic inflammation as well as local, we studied lung expression of one of the most

important proinflammatory cytokines, interleukin-1β. We found that LPS drastically augments *de novo* production of pro-IL-1β, whereas Ab/(Ft/SOD) significantly blocks LPS-mediated pro-IL-1β synthesis, disrupting the initial step of the IL-1β cascade (Fig. 13).

4. Discussion

Endothelial cells directly exposed to the bloodstream represent an attractive target for drug delivery that can be achieved in animals and in human organs via conjugating drugs or their carriers with antibodies, scFv fragments and other affinity ligands providing anchoring on appropriate endothelial surface determinants [46]. Not all endothelial targets, however, are freely accessible to their ligands, especially when the ligand is coupled to the surface of a carrier, whose size can impose steric hindrance in nanoparticle interaction with partially hidden target molecules.

Superoxide fluxes in the endosomal lumen by NADPH oxidase in response to the interaction of cytokines and microbial components to cognate endothelial cell receptors such as TLR4, ignites NFκB-mediated pathological cellular activation, e.g., expression of VCAM-1 and other adhesion molecules propagating inflammation [27,47]. The compartmentalized nature of this pathway provides a conceptual framework for designing precise anti-inflammatory nanomedicine [24] using endosomal targeting of SOD [25,29,48]. Ideally, SOD targeting should be delivered and act selectively in the type(s) of endosomes implicated in given pathological pathway. This level of sub-cellular precision encompasses several aspects of drug targeting. First, selected binding or anchoring site must direct the carrier into the appropriate type of endosomes [25,28,29].

Caveolae and caveolar endosomes are involved in superoxide signaling caused by TNF, LPS and other agents acting via the cholesterol-rich domains in the membrane [49–51]. The inflammatory effect of LPS is attenuated in caveolin-1 knockout mice, supporting the notion that targeting SOD into caveolar endosomes provides a mechanism of precise inhibition of this pathway [52]. Targeting SOD to endosomes via caveolae may boost efficacy and specificity of blocking pro-inflammatory changes induced by TLR4 agonist. However, it’s important to keep in mind that internalization of caveolae-targeted nanoparticles may occur by different mechanisms, not necessarily by caveolar endocytosis. Earlier we demonstrated efficacy of Plvap targeting in delivery of antioxidant enzyme as anti-inflammatory agent using antibody-enzyme protein conjugate [28]. However, drug-loaded nanoparticles have several potential advantages compared to antibody-enzyme conjugates. Multimolecular nature of the nanoparticle allows much higher avidity of the drug-delivery system to the target and fast internalization due to target clusterization. In addition, loading the drug inside the nanocage (as in Ab/(Ft/SOD) nanocages in this study) keeps particle surface available for affinity moiety and may protect biotherapeutics from potentially damaging blood and intracellular environments.

Further, molecular configuration of functional moieties should yield a drug delivery system with optimally harmonized targeting and effect functions [53], while not exceeding the size constraints of this type of endosomes [54]. To achieve this goal, we combined several novel aspects of nanocarrier design that mutually fortify the utility of this platform technology for

caveolar drug delivery. Caveolar delivery is desirable for SOD (and likely other drugs) but the caveolar average external diameter is 60–80 nm [55,56] and aperture diameter is ca. 30–50 nm [57]. It should be noted that due to the dynamic and polymorphic character of these vesicles, a range of opening diameters should be expected [57]. Moreover, there is some mismatch between the size of the opening in fixed and unfixed tissue [58]. In addition, it likely also varies depending on the state of the cells and characteristics of the particles including, but not limited to their size and shape. For example, there were reports of the uptake of particles as large as 100 nm by caveolae-related pathway *in vitro* [59]. It should be noted, however, that features of caveolar endocytosis can be altered in cell culture, like many other cellular functions. A prolonged incubation of large doses of particles with serum-deprived static cells may lead to indiscriminate uptake via pathways that are unlikely to operate *in vivo.* In this context, pulmonary uptake and the effect of particles targeted to caveolar determinants seems to be more physiologically relevant surrogate readout. Our previous *in vivo* studies revealed that caveolae-targeted rigid spherical particles larger than 70–90 nm do not accumulate in the lungs [18]. In contrast, elastic parameters of the carriers seem even more important than size: flexible nanogels with mean diameter 300 nm do get internalized via caveolar pathway(s) and accumulate effectively in the lungs [60]. However, the nanocarriers used in the present study are smaller than the caveolar aperture, and, therefore, the key parameter controlling targeting in this case is particle avidity.

Thus, using Plvap-1 as the anchoring determinant enables highly efficient targeting to the pulmonary vasculature according to direct isotope tracing *in vivo.* Fluorescence microscopy of cultured cells shows that nanocarriers are rapidly taken up by endothelial cells. Plvap-1 is a component of endothelial caveolae and fenestrations [61]. It is found primarily in capillaries and venules in many tissues except for the brain, with the highest level in tissues including lungs, kidney, liver and some tumors [62,63].

We demonstrated that Plvap-targeted ferritin-based nanoparticles readily binds to caveolae, internalized with quick dissociation from caveolin-containing vesicles. The nanoparticles effectively deliver preloaded drug to endosomes that remains in the endosomal lumen for up to 24 h and potentially longer (unpublished observations). Precise attribution of the binding domain(s), type(s) of endocytic vesicles and itinerary of intracellular traffic of Plvap-1 targeted nanocarriers and their iterations is worth subsequent mechanistic studies. Cell cultures do not fully recapitulate the state of affairs *in vivo*. Resolution and specificity of current methods are insufficient for direct studies of this aspect *in vivo* in an accurate and quantitative manner. Further we showed that our caveolae-targeted drug delivery system can effectively block pro-inflammatory effects of LPS in animals. Collectively *in vitro* and *in vivo* data shown in this paper are consistent with Pvlap-targeted nanoparticles delivering SOD to caveolar endosomes, which results in alleviation of the inflammatory effect of LPS in an animal model of endotoxemia.

5. Conclusions

Ferritin nanoparticles provide advantageous carriers for caveolar delivery. Small and uniform size, versatile yet sturdy structural features permitting diverse genetic and chemical modifications, and controlled reversible disassembly and re-assembly all represent very

attractive characteristics. In particular, these features support configuration of the tri-molecular complexes with spatially optimized conjugation of the cargo and ligand, yielding an effective drug delivery system with resultant size, affinity and payload meeting the intended goal.

Supplementary Material

Refer to Web version on PubMed Central for supplementary material.

Acknowledgments

This work was supported by the National Institutes of Health [Grant RO1 HL073940] (to V.R.M.), [Grant NCATS UL1TR000003] ITMAT Pilot Grant (to V.V.S.), and National Science Foundation [Grant NSF CHE-1508318] (to K.W.P. and I.J.D.).

References

[1]. Perry JL, Kai MP, Reuter KG, Bowerman C, Christopher Luft J, DeSimone JM, Calibration-quality cancer nanotherapeutics, Canc. Treat Res 166 (2015) 275–291.

[2]. Kelley WJ, Safari H, Lopez-Cazares G, Eniola-Adefeso O, Vascular-targeted nanocarriers: design considerations and strategies for successful treatment of atherosclerosis and other vascular diseases, Wiley Interdiscip. Rev. Nanomed. Nanobiotechnol 8 (6) (2016) 909–926. [PubMed: 27194461]

[3]. Jordan C, Shuvaev VV, Bailey M, Muzykantov VR, Dziubla TD, The role of Carrier geometry in overcoming biological barriers to drug delivery, Curr. Pharmaceut. Des 22 (9) (2016) 1259–1273.

[4]. Mitragotri S, Burke PA, Langer R, Overcoming the challenges in administering biopharmaceuticals: formulation and delivery strategies, Nat. Rev. Drug Discov 13 (9) (2014) 655–672. [PubMed: 25103255]

[5]. Komarova Y, Malik AB, Regulation of endothelial permeability via paracellular and transcellular transport pathways, Annu. Rev. Physiol. 72 (2010) 463–493. [PubMed: 20148685]

[6]. Bagam P, Singh DP, Inda ME, Batra S, Unraveling the role of membrane microdomains during microbial infections, Cell Biol. Toxicol. 33 (5) (2017) 429–455. [PubMed: 28275881]

[7]. Van Krieken R, Krepinsky JC, Caveolin-1 in the pathogenesis of diabetic nephropathy: potential therapeutic target? Curr. Diabetes Rep. 17 (3) (2017) 19.

[8]. Parton RG, del Pozo MA, Caveolae as plasma membrane sensors, protectors and organizers, Nat. Rev. Mol. Cell Biol. 14 (2) (2013) 98–112. [PubMed: 23340574]

[9]. Chrastina A, Valadon P, Massey KA, Schnitzer JE, Lung vascular targeting using antibody to aminopeptidase P: CT-SPECT imaging, biodistribution and pharmacokinetic analysis, J. Vasc. Res 47 (6) (2010) 531–543. [PubMed: 20431301]

[10]. Massey KA, Schnitzer JE, Targeting and imaging signature caveolar molecules in lungs, Proc. Am. Thorac. Soc. 6 (5) (2009) 419–430. [PubMed: 19687214]

[11]. Oh P, Borgstrom P, Witkiewicz H, Li Y, Borgstrom BJ, Chrastina A, Iwata K, Zinn KR, Baldwin R, Testa JE, Schnitzer JE, Live dynamic imaging of caveolae pumping targeted antibody rapidly and specifically across endothelium in the lung, Nat. Biotechnol. 25 (3) (2007) 327–337. [PubMed: 17334358]

[12]. Oh P, Testa JE, Borgstrom P, Witkiewicz H, Li Y, Schnitzer JE, In vivo proteomic imaging analysis of caveolae reveals pumping system to penetrate solid tumors, Nat. Med. 20 (9) (2014) 1062–1068. [PubMed: 25129480]

[13]. Tichauer KM, Deharvengt SJ, Samkoe KS, Gunn JR, Bosenberg MW, Turk MJ, Hasan T, Stan RV, Pogue BW, Tumor endothelial marker imaging in melanomas using dual-tracer fluorescence molecular imaging, Mol. Imag. Biol 16 (3) (2014) 372–382.

[14]. Elgueta R, Tse D, Deharvengt SJ, Luciano MR, Carriere C, Noelle RJ, Stan RV, Endothelial plasmalemma vesicle-associated protein regulates the homeostasis of splenic immature B cells and B-1 B cells, J. Immunol. 197 (10) (2016) 3970–3981. [PubMed: 27742829]

[15]. Stan RV, Structure of caveolae, Biochim. Biophys. Acta 1746 (3) (2005) 334–348. [PubMed: 16214243]

[16]. Stan RV, Kubitza M, Palade GE, PV-1 is a component of the fenestral and stomatal diaphragms in fenestrated endothelia, Proc. Natl. Acad. Sci. U. S. A. 96 (23) (1999) 13203–13207. [PubMed: 10557298]

[17]. Tkachenko E, Tse D, Sideleva O, Deharvengt SJ, Luciano MR, Xu Y, McGarry CL, Chidlow J, Pilch PF, Sessa WC, Toomre DK, Stan RV, Caveolae, fenestrae and transendothelial channels retain PV1 on the surface of endothelial cells, PLoS One 7 (3) (2012) e32655. [PubMed: 22403691]

[18]. Simone EA, Zern BJ, Chacko AM, Mikitsh JL, Blankemeyer ER, Muro S, Stan RV, Muzykantov VR, Endothelial targeting of polymeric nanoparticles stably labeled with the PET imaging radioisotope iodine-124, Biomaterials 33 (21) (2012) 5406–5413. [PubMed: 22560201]

[19]. Wang Z, Tiruppathi C, Cho J, Minshall RD, Malik AB, Delivery of nanoparticle: complexed drugs across the vascular endothelial barrier via caveolae, IUBMB Life 63 (8) (2011) 659–667. [PubMed: 21766412]

[20]. He D, Marles-Wright J, Ferritin family proteins and their use in bionanotechnology, N. Biotech 32 (6) (2015) 651–657.

[21]. Charlton JR, Pearl VM, Denotti AR, Lee JB, Swaminathan S, Scindia YM, Charlton NP, Baldelomar EJ, Beeman SC, Bennett KM, Biocompatibility of ferritin-based nanoparticles as targeted MRI contrast agents, Nanomedicine 12 (6) (2016) 1735–1745. [PubMed: 27071333]

[22]. Khoshnejad M, Parhiz H, Shuvaev VV, Dmochowski IJ, Muzykantov VR, Ferritin-based drug delivery systems: hybrid nanocarriers for vascular immunotargeting, J. Contr. Release 282 (2018) 13–24.

[23]. Swift J, Butts CA, Cheung-Lau J, Yerubandi V, Dmochowski IJ, Efficient self-assembly of Archaeoglobus fulgidus ferritin around metallic cores, Langmuir 25 (9) (2009) 5219–5225. [PubMed: 19260687]

[24]. Shuvaev VV, Muzykantov VR, Targeted modulation of reactive oxygen species in the vascular endothelium, J. Contr. Release 153 (1) (2011) 56–63.

[25]. Shuvaev VV, Han J, Tliba S, Arguiri E, Christofidou-Solomidou M, Ramirez SH, Dykstra H, Persidsky Y, Atochin DN, Huang PL, Muzykantov VR, Anti-inflammatory effect of targeted delivery of SOD to endothelium: mechanism, synergism with NO donors and protective effects in vitro and in vivo, PLoS One 8 (10) (2013) e77002. [PubMed: 24146950]

[26]. Oakley FD, Smith RL, Engelhardt JF, Lipid rafts and caveolin-1 coordinate interleukin-1beta (IL-1beta)-dependent activation of NFkappaB by controlling endocytosis of Nox2 and IL-1beta receptor 1 from the plasma membrane, J. Biol. Chem. 284 (48) (2009) 33255–33264. [PubMed: 19801678]

[27]. Spencer NY, Engelhardt JF, The basic biology of redoxosomes in cytokine-mediated signal transduction and implications for disease-specific therapies, Biochemistry 53 (10) (2014) 1551–1564. [PubMed: 24555469]

[28]. Shuvaev VV, Kiseleva RY, Arguiri E, Villa CH, Muro S, Christofidou-Solomidou M, Stan RV, Muzykantov VR, Targeting superoxide dismutase to endothelial caveolae profoundly alleviates inflammation caused by endotoxin, J. Contr. Release 272 (2018) 1–8.

[29]. Shuvaev VV, Han J, Yu KJ, Huang S, Hawkins BJ, Madesh M, Nakada M, Muzykantov VR, PECAM-targeted delivery of SOD inhibits endothelial inflammatory response, Faseb. J. 25 (1) (2011) 348–357. [PubMed: 20876216]

[30]. Pulsipher KW, Dmochowski IJ, Ferritin encapsulation and templated synthesis of inorganic nanoparticles, Meth. Mol. Biol. 1252 (2015) 27–37.

[31]. Pulsipher KW, Honig S, Deng S, Dmochowski IJ, Controlling gold nanoparticle seeded growth in thermophilic ferritin protein templates, J. Inorg. Biochem. 174 (2017) 169–176. [PubMed: 28683348]

[32]. McCord JM, Fridovich I, Superoxide dismutase. An enzymic function for erythrocuprein (hemocuprein), J. Biol. Chem. 244 (22) (1969) 6049–6055. [PubMed: 5389100]

[33]. Khoshnejad M, Shuvaev VV, Pulsipher KW, Dai C, Hood ED, Arguiri E, Christofidou-Solomidou M, Dmochowski IJ, Greineder CF, Muzykantov VR, Vascular accessibility of endothelial targeted ferritin nanoparticles, Bioconjugate Chem. 27 (3) (2016) 628–637.

[34]. Muro S, Muzykantov VR, Murciano JC, Characterization of endothelial internalization and targeting of antibody-enzyme conjugates in cell cultures and in laboratory animals, Meth. Mol. Biol. 283 (2004) 21–36.

[35]. Wiewrodt R, Thomas AP, Cipelletti L, Christofidou-Solomidou M, Weitz DA, Feinstein SI, Schaffer D, Albelda SM, Koval M, Muzykantov VR, Size-dependent intracellular immunotargeting of therapeutic cargoes into endothelial cells, Blood 99 (3) (2002) 912–922. [PubMed: 11806994]

[36]. Manders EMM, Verbeek FJ, Aten JA, Measurement of co-localization of objects in dual-colour confocal images, J. Microsc. 169 (3) (1993) 375–382.

[37]. Johnson E, Cascio D, Sawaya MR, Gingery M, Schroder I, Crystal structures of a tetrahedral open pore ferritin from the hyperthermophilic archaeon Archaeoglobus fulgidus, Structure 13 (4) (2005) 637–648. [PubMed: 15837202]

[38]. Cheung-Lau JC, Liu D, Pulsipher KW, Liu W, Dmochowski IJ, Engineering a well-ordered, functional protein-gold nanoparticle assembly, J. Inorg. Biochem. 130 (2014) 59–68. [PubMed: 24176920]

[39]. Pulsipher KW, Villegas JA, Roose BW, Hicks TL, Yoon J, Saven JG, Dmochowski IJ, Thermophilic ferritin 24mer assembly and nanoparticle encapsulation modulated by interdimer electrostatic repulsion, Biochemistry 56 (28) (2017) 3596–3606. [PubMed: 28682599]

[40]. Khoshnejad M, Greineder CF, Pulsipher KW, Villa CH, Altun B, Pan DC, Tsourkas A, Dmochowski IJ, Muzykantov VR, Ferritin nanocages with biologically orthogonal conjugation for vascular targeting and imaging, Bioconjugate Chem. 29 (4) (2018) 1209–1218.

[41]. Oh P, McIntosh DP, Schnitzer JE, Dynamin at the neck of caveolae mediates their budding to form transport vesicles by GTP-driven fission from the plasma membrane of endothelium, J. Cell Biol. 141 (1) (1998) 101–114. [PubMed: 9531551]

[42]. Schnitzer JE, Oh P, McIntosh DP, Role of GTP hydrolysis in fission of caveolae directly from plasma membranes, Science 274 (5285) (1996) 239–242. [PubMed: 8824187]

[43]. Schnitzer JE, McIntosh DP, Dvorak AM, Liu J, Oh P, Separation of caveolae from associated microdomains of GPI-anchored proteins, Science 269 (5229) (1995) 1435–1439. [PubMed: 7660128]

[44]. Scherpereel A, Rome JJ, Wiewrodt R, Watkins SC, Harshaw DW, Alder S, Christofidou-Solomidou M, Haut E, Murciano JC, Nakada M, Albelda SM, Muzykantov VR, Platelet-endothelial cell adhesion molecule-1-directed immunotargeting to cardiopulmonary vasculature, J. Pharmacol. Exp. Therapeut 300 (3) (2002) 777–786.

[45]. Zern BJ, Chacko AM, Liu J, Greineder CF, Blankemeyer ER, Radhakrishnan R, Muzykantov V, Reduction of nanoparticle avidity enhances the selectivity of vascular targeting and PET detection of pulmonary inflammation, ACS Nano 7 (3) (2013) 2461–2469. [PubMed: 23383962]

[46]. Howard MD, Hood ED, Zern B, Shuvaev VV, Grosser T, Muzykantov VR, Nanocarriers for vascular delivery of anti-inflammatory agents, Annu. Rev. Pharmacol. Toxicol. 54 (2014) 205–226. [PubMed: 24392694]

[47]. Ushio-Fukai M, Compartmentalization of redox signaling through NADPH oxidase-derived ROS, Antioxidants Redox Signal. 11 (6) (2009) 1289–1299.

[48]. Hood ED, Greineder CF, Dodia C, Han J, Mesaros C, Shuvaev VV, Blair IA, Fisher AB, Muzykantov VR, Antioxidant protection by PECAM-targeted delivery of a novel NADPH-oxidase inhibitor to the endothelium in vitro and in vivo, J. Contr. Release 163 (2) (2012) 161–169.

[49]. Guillot L, Medjane S, Le-Barillec K, Balloy V, Danel C, Chignard M, Si-Tahar M, Response of human pulmonary epithelial cells to lipopolysaccharide involves Toll-like receptor 4 (TLR4)-dependent signaling pathways: evidence for an intracellular compartmentalization of TLR4, J. Biol. Chem. 279 (4) (2004) 2712–2718. [PubMed: 14600154]

[50]. Hornef MW, Normark BH, Vandewalle A, Normark S, Intracellular recognition of lipopolysaccharide by toll-like receptor 4 in intestinal epithelial cells, J. Exp. Med. 198 (8) (2003) 1225–1235. [PubMed: 14568981]

[51]. Pascual-Lucas M, Fernandez-Lizarbe S, Montesinos J, Guerri C, LPS or ethanol triggers clathrin- and rafts/caveolae-dependent endocytosis of TLR4 in cortical astrocytes, J. Neurochem. 129 (3) (2014) 448–462. [PubMed: 24345077]

[52]. Garrean S, Gao XP, Brovkovych V, Shimizu J, Zhao YY, Vogel SM, Malik AB, Caveolin-1 regulates NF-kappaB activation and lung inflammatory response to sepsis induced by lipopolysaccharide, J. Immunol. 177 (7) (2006) 4853–4860. [PubMed: 16982927]

[53]. Okeley NM, Alley SC, Senter PD, Advancing antibody drug conjugation: from the laboratory to a clinically approved anticancer drug, Hematol. Oncol. Clin. N. Am 28 (1) (2014) 13–25.

[54]. Shuvaev VV, Muro S, Arguiri E, Khoshnejad M, Tliba S, Christofidou-Solomidou M, Muzykantov VR, Size and targeting to PECAM vs ICAM control endothelial delivery, internalization and protective effect of multimolecular SOD conjugates, J. Contr. Release 234 (2016) 115–123.

[55]. Predescu SA, Predescu DN, Malik AB, Molecular determinants of endothelial transcytosis and their role in endothelial permeability, Am. J. Physiol. Lung Cell Mol. Physiol 293 (4) (2007) L823–L842. [PubMed: 17644753]

[56]. McIntosh DP, Tan XY, Oh P, Schnitzer JE, Targeting endothelium and its dynamic caveolae for tissue-specific transcytosis in vivo: a pathway to overcome cell barriers to drug and gene delivery, Proc. Natl. Acad. Sci. U. S. A. 99 (4) (2002) 1996–2001. [PubMed: 11854497]

[57]. Lebbink MN, Jimenez N, Vocking K, Hekking LH, Verkleij AJ, Post JA, Spiral coating of the endothelial caveolar membranes as revealed by electron tomography and template matching, Traffic 11 (1) (2010) 138–150. [PubMed: 20002353]

[58]. Noguchi Y, Shibata Y, Yamamoto T, Endothelial vesicular system in rapid-frozen muscle capillaries revealed by serial sectioning and deep etching, Anat. Rec. 217 (4) (1987) 355–360. [PubMed: 3592261]

[59]. Wang Z, Tiruppathi C, Minshall RD, Malik AB, Size and dynamics of caveolae studied using nanoparticles in living endothelial cells, ACS Nano 3 (12) (2009) 4110–4116. [PubMed: 19919048]

[60]. Myerson JW, Braender B, McPherson O, Glassman PM, Kiseleva RY, Shuvaev VV, Marcos-Contreras O, Grady ME, Lee HS, Greineder CF, Stan RV, Composto RJ, Eckmann DM, Muzykantov VR, Flexible nanoparticles reach sterically obscured endothelial targets inaccessible to rigid nanoparticles, Adv. Mater. 30 (32) (2018) e1802373. [PubMed: 29956381]

[61]. Tse D, Stan RV, Morphological heterogeneity of endothelium, Semin. Thromb. Hemost 36 (3) (2010) 236–245. [PubMed: 20490976]

[62]. Strickland LA, Jubb AM, Hongo JA, Zhong F, Burwick J, Fu L, Frantz GD, Koeppen H, Plasmalemmal vesicle-associated protein (PLVAP) is expressed by tumour endothelium and is upregulated by vascular endothelial growth factor-A (VEGF), J. Pathol. 206 (4) (2005) 466–475. [PubMed: 15971170]

[63]. Stan RV, Arden KC, Palade GE, cDNA and protein sequence, genomic organization, and analysis of cis regulatory elements of mouse and human PLVAP genes, Genomics 72 (3) (2001) 304–313. [PubMed: 11401446]

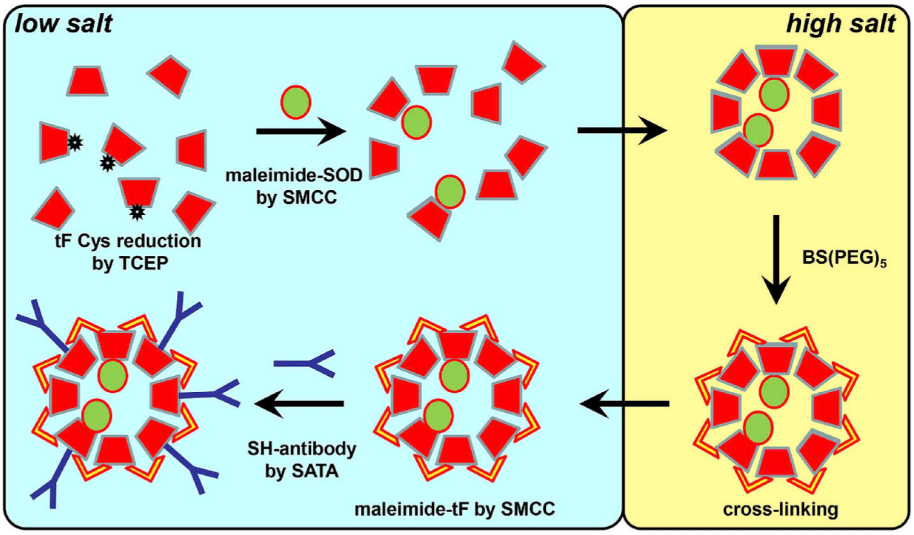

Fig. 1. Scheme reaction of Ab/(Ft/SOD) preparation.

Single-cysteine-containing thermophilic ferritin was reduced by TCEP, conjugated with maleimide-SOD, and then transferred to high salt to reassemble and to cross-link used $BS(PEG)_5$. Crosslinked ferritin was transferred back to low salt and antibody or control IgG were conjugated to the surface of reassembled particles using standard amino chemistry as described in Methods.

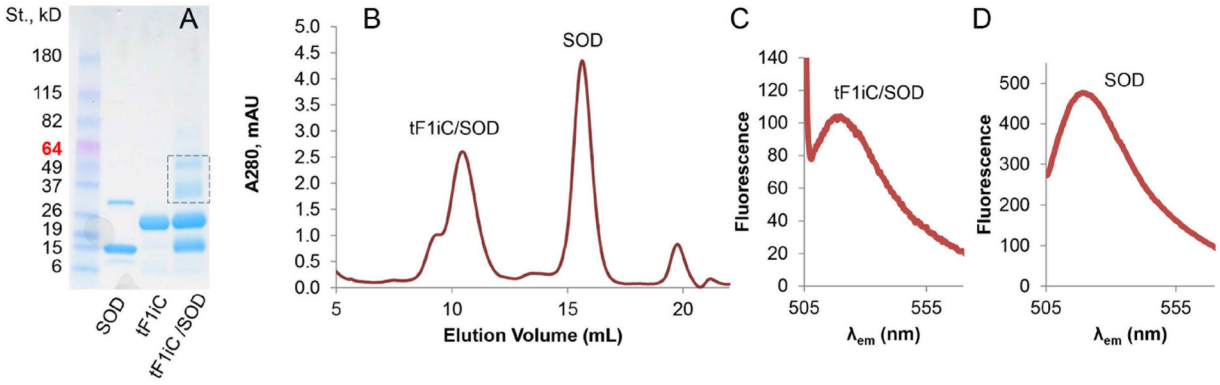

Fig. 2. Conjugation of SOD to thermophilic ferritin.

Single-cysteine-containing thermophilic ferritin tF1iC was disassembled in PBS and cysteines were reduced. Maleimide groups were introduced into Alexa 488 Fluor labeled SOD and SOD was conjugated to the PBS. Then conjugates were transferred to high-salt buffer to reassemble ferritin nanocage structure. Unreacted SOD was removed using FPLC while the ferritin-containing peak was collected and analyzed for the presence of SOD. (A). SDS-PAGE of tF1iC/SOD conjugation. (B). FPLC of tF1iC/SOD mixture in high salt (PBS/0.8 M NaCl). (C-D). Alexa Fluor 488 fluorescence of tF1iC/SOD (C) and unbound SOD (D) peaks.

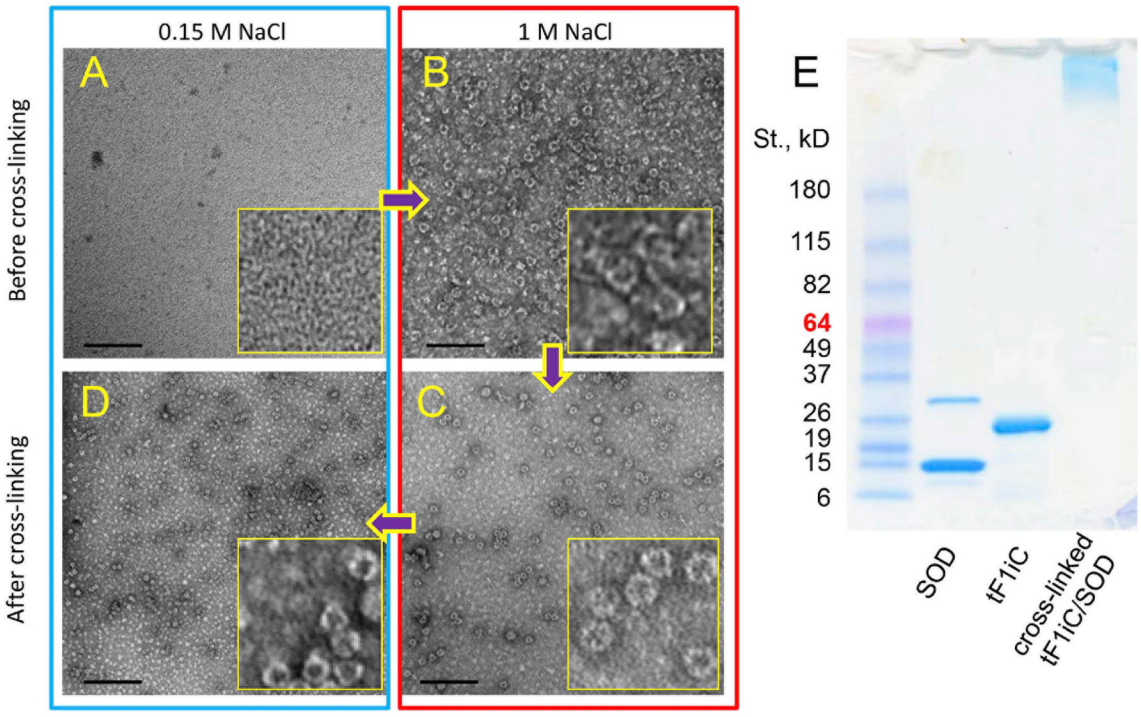

Fig. 3. Crosslinking of tF1iC.

To prevent tF1iC/SOD from disassembling after transfer back to physiological (i.e. low-salt) buffer (such as PBS) ferritin was treated with crosslinking agent $BS(PEG)_5$ in high salt (1 M NaCl). (A-D). TEM: (A) tF1iC/SOD in low salt; (B) tF1iC/SOD in high salt; (C) crosslinked tF1iC/SOD in high salt; (D) crosslinked tF1iC/SOD in low salt. 200,000× magnification, bar = 100 nm. (E). 4–15% gradient Tris-glycine SDS-PAGE of cross-linked tF1iC/SOD. Free SOD was removed using FPLC before crosslinking.

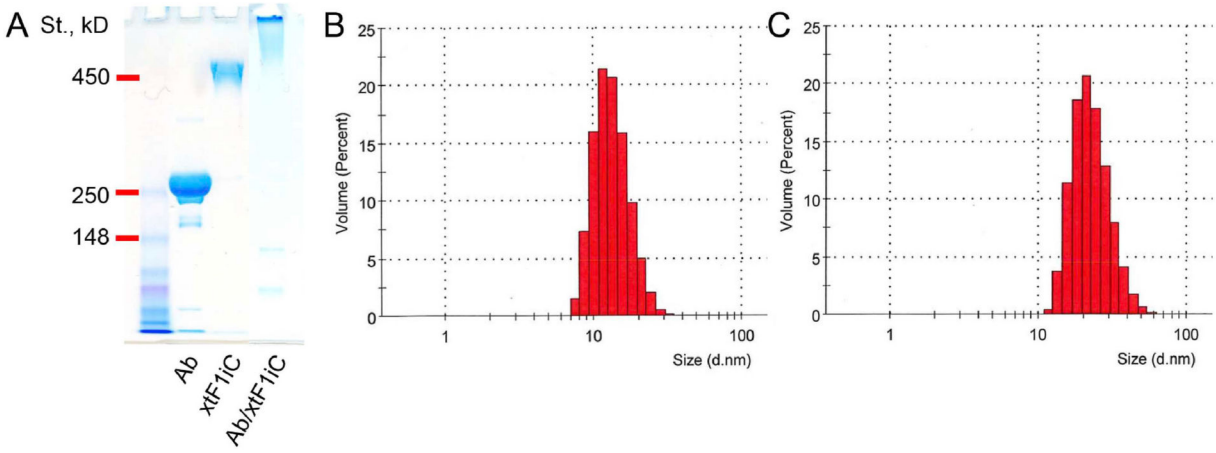

Fig. 4. Characterization of crosslinked thermophilic single cysteine ferritin tF1iC coated with targeting antibody (i.e., Ab/(Ft/SOD) in the text).

Crosslinked tF1iC/SOD was conjugated with antibody to Plvap using amino-chemistry. (A). 3–8% NuPAGE Tris-acetate non-reducing SDS-gel electrophoresis. DLS size distribution analysis of crosslinked tF1iC/SOD before (B) and after (C) coating with antibody. Unbound antibodies as well as free light and heavy IgG chains seen on SDS-electrophoresis were separated by FPLC.

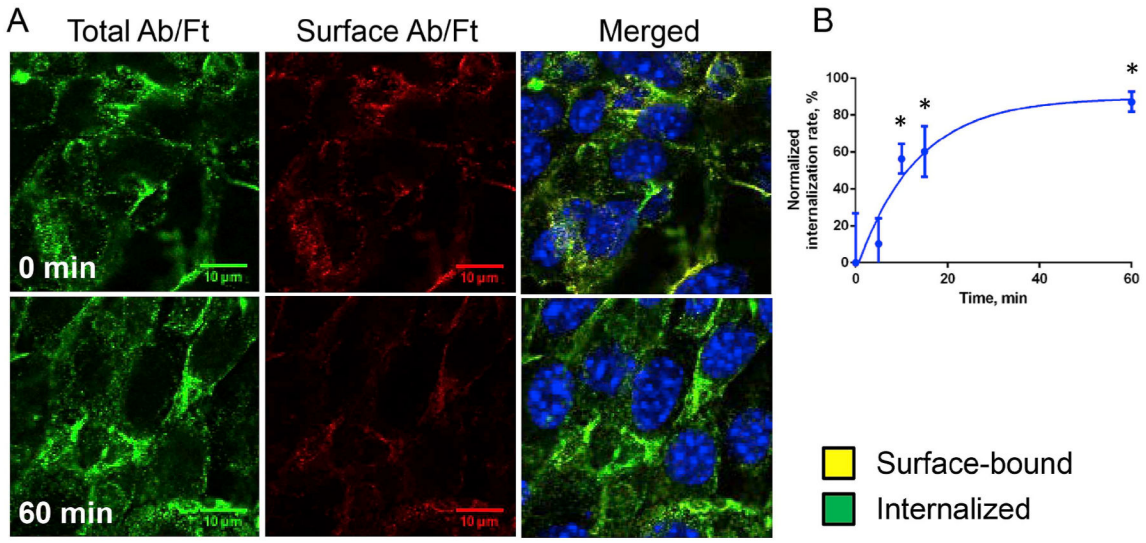

Fig. 5. Internalization of Plvap-directed Ab/(Ft/SOD) by murine endothelial cells.

(A). Endothelial bEnd3 cells were incubated with conjugates on ice for 2 h, washed and transferred to 37 °C for indicated periods of time. On the merged panels green and yellow colors are internalized and surface-bound particles, respectively. Nuclei were stained with DAPI (blue). Confocal microscopy. Scale bar is 20 μm. (B). Quantification analysis of internalization rate (see Methods for details), n = 3, mean ± SD are shown. Data was normalized by initial time point; *P < 0.05 vs. 0 min time point. (For interpretation of the references to color in this figure legend, the reader is referred to the Web version of this article.)

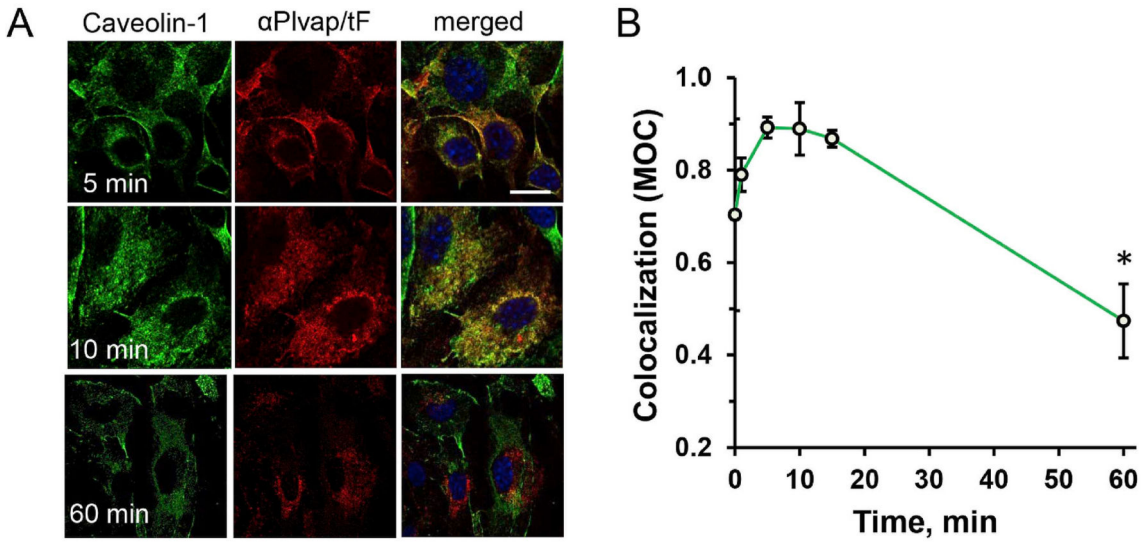

Fig. 6. Kinetics of Plvap-directed Ab/(Ft/SOD) co-localization with caveolin-1.

Endothelial cells bEnd3 were incubated with nanoparticles on ice for 2 h, washed and incubated for up to 60 min at 37 °C. (A). Co-staining of caveolin-1 (green) and nanoparticles (red). Nuclei were stained with DAPI (blue). Scale bar is 20 μm. (B). Menders' Overlap Coefficient (MOC) of nanoparticles vs. caveolin-1 co-localization. Confocal microscopy; n of fields ≥6; mean ± SD are shown; *P < 0.05 vs. initial time point. (For interpretation of the references to color in this figure legend, the reader is referred to the Web version of this article.)

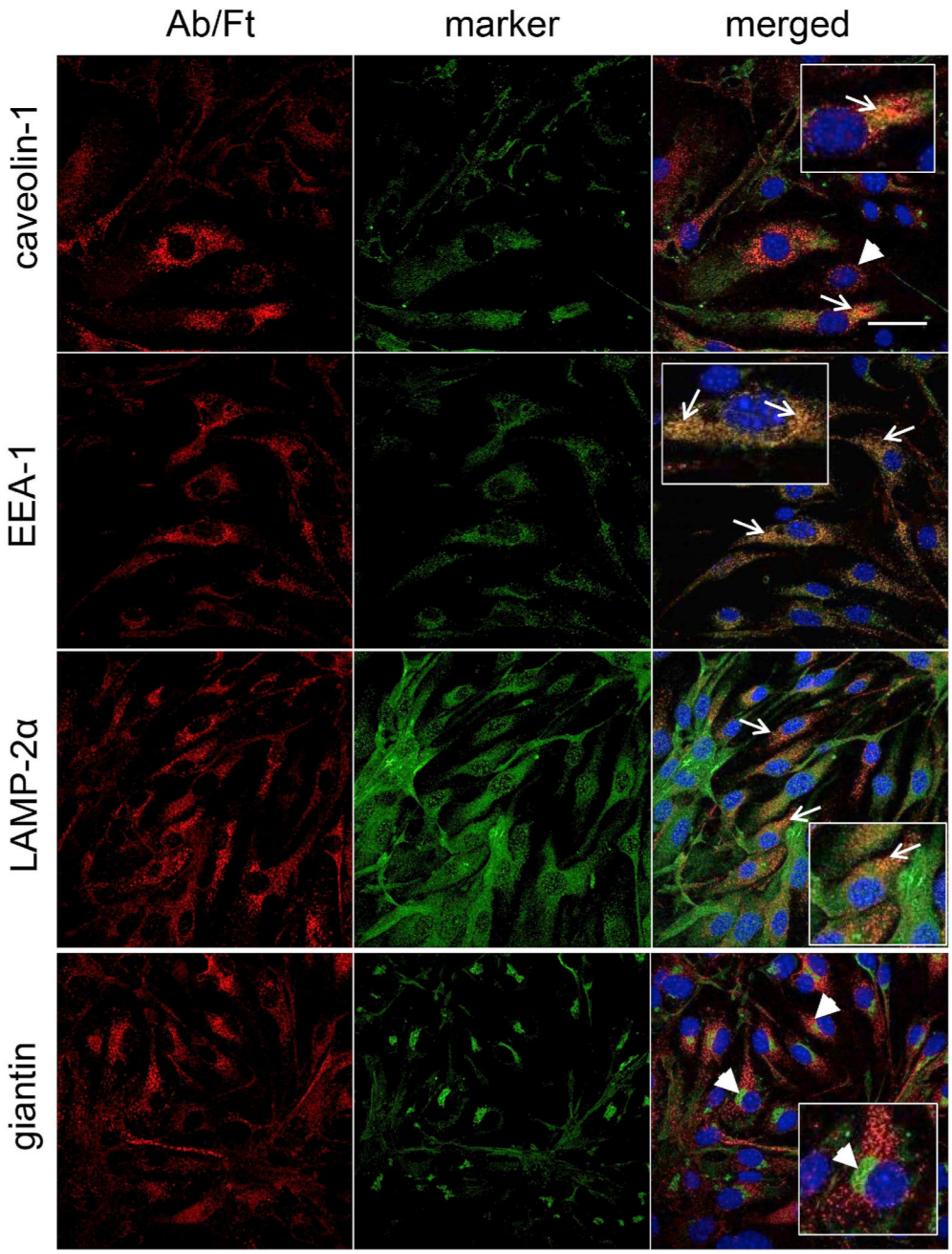

Fig. 7. Co-localization of Plvap-directed Ab/(Ft/SOD) with cellular organelles.

Cells were incubated with nanoparticles for 1 h at 37 °C, washed, fixed, permeabilized and stained for the ferritin nanoparticles with labeled secondary anti-rat IgG (red) and the following markers (all are in green): caveolin-1 (caveolae), EEA-1 (endosomes), LAMP-2α (lysosomes), giantin (Golgi). Nuclei were stained with DAPI (blue). Representative images correspond to 0.3-μm slice. Yellow-colored area indicates colocalization of nanoparticles and organelle. Arrows show co-localization of nanoparticles with organelle marker, arrow heads - no co-localization. Zoomed views are inserted in merged panels. Confocal

microscopy. (For interpretation of the references to color in this figure legend, the reader is referred to the Web version of this article.)

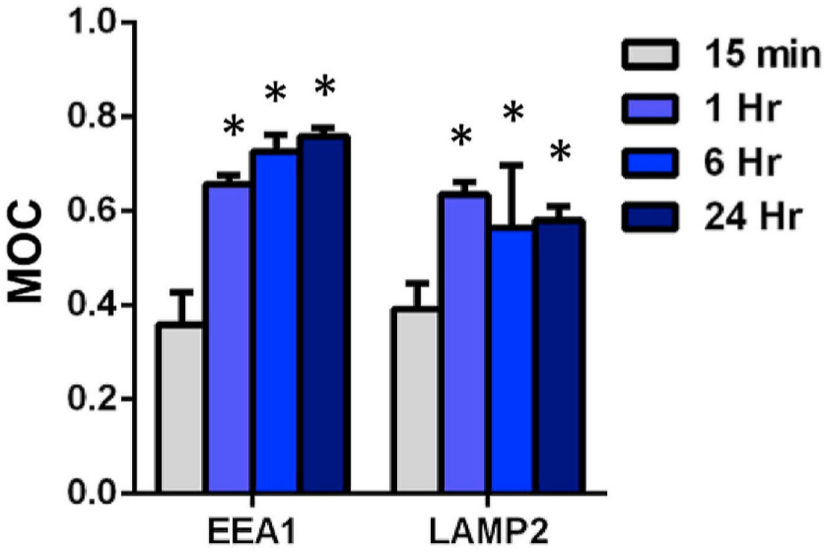

Fig. 8. Trafficking of Plvap-directed Ab/(Ft/SOD) to cellular destinations.

Cells were incubated with nano particles from 15 min to 24 h at 37 °C, washed, fixed, permeabilized and stained for EEA-1 (endosomes) and LAMP-2α (lysosomes). MOC of nanoparticles vs. marker of potential destination. Confocal microscopy; n of fields ≥6; mean ± SD are shown; *P < 0.05 vs. 15 min time point.

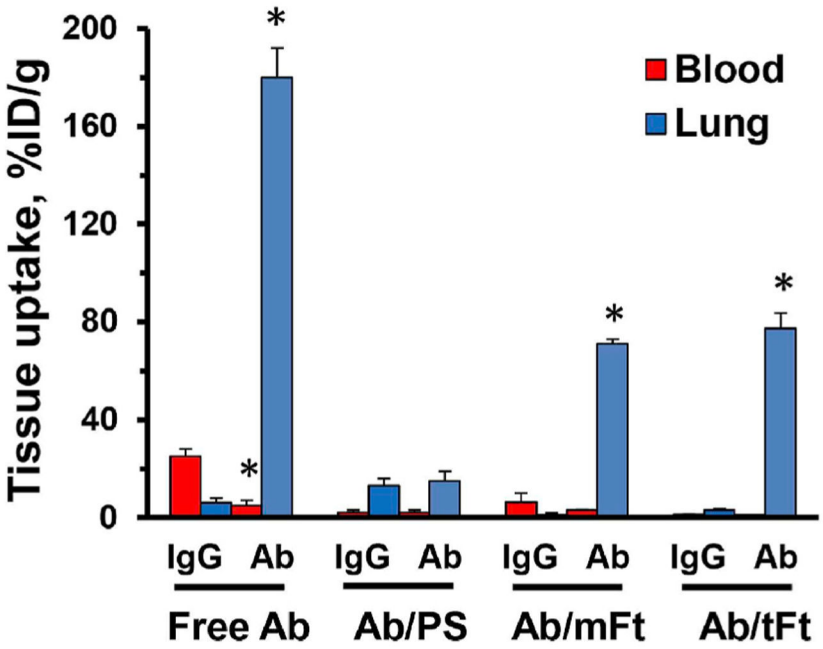

Fig. 9. Pulmonary targeting of anti-Plvap and Plvap-targeted nanoparticles in mice.

Blood and lung level 1 h after IV injection in mice of radiolabeled Plvap antibody, or with 200-nm polystyrene particles carrying the same Ab (PS), or ^{125}I-Ft particles formulated with mammalian ferritin (*m*Ft) and thermophilic ferritin (*t*Ft) carrying the same antibody. To avoiding artifact of tracing ligand that might dissociate from the nanocarriers, they were traced using 10mol% of ^{125}I-labeled control IgG admixed to non-labeled Plvap Ab. Mean ± SD are shown; *P < 0.05 Ab vs. IgG.

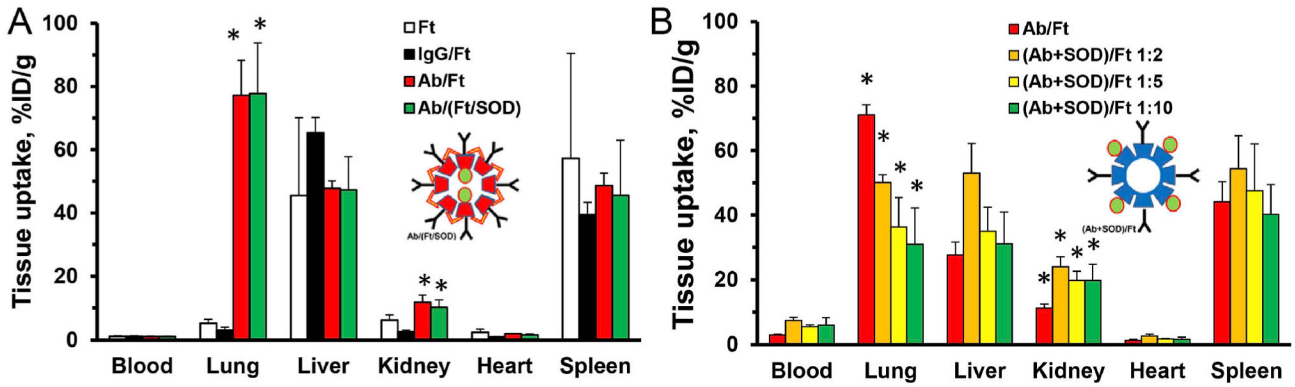

Fig. 10. Tissue accumulation of Plvap-targeted ferritin-based nanocages.

Comparison of Ft particles with SOD loaded either inside Ab/(Ft/SOD) (A) or outside (Ab + SOD)/Ft (B) the particles. Tissues were harvested 1 h post-injection. (A). Thermophilic Ft was crosslinked and coated with either non-immune control IgG (IgG/Ft) or anti-Plvap antibody SOD-free (Ab/Ft) or SOD loaded inside the particles Ab/(Ft/SOD). (B). Mammalian Ft was coated either with anti-Plvap (Ab/Ft) or with combination of antibody and SOD ((Ab + SOD)/Ft) at indicated Ab:SOD molar ratio. Insets show schematic presentations of the corresponding nanocages. Mean ± SD are shown; *P < 0.05 Ab vs. IgG.

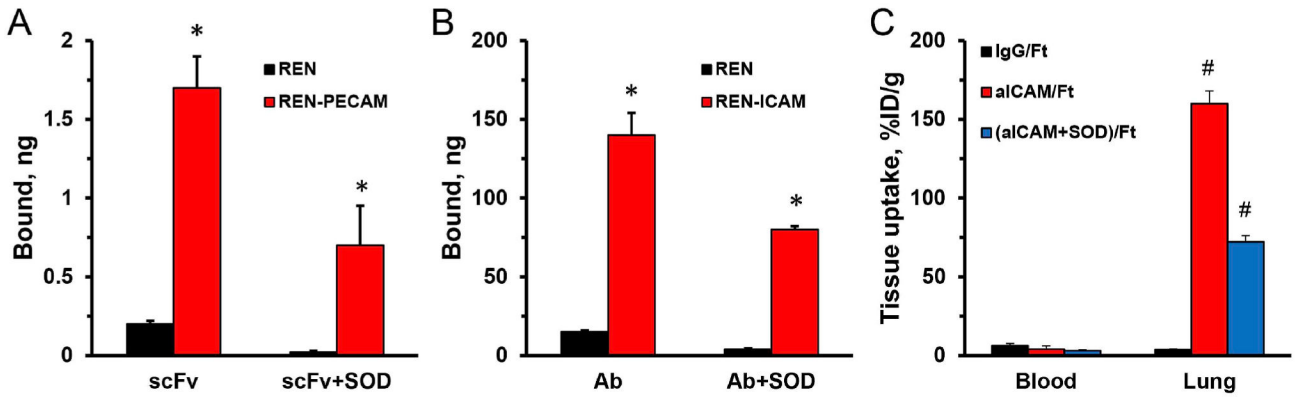

Fig. 11. Binding of targeted Ft and Ft-SOD conjugates *in vitro* and *in vivo*.

(A-B). Ab/Ft or (Ab + SOD)/Ft containing radiolabeled ferritin were incubated with antigen-negative or antigen-positive REN cells for 1 h at 37 °C. Bound nanocarrier fraction was measured by gamma counter. (A). Nanocarriers with anti-PECAM scFv binding to PECAM-negative or PECAM-positive REN cells; 170 ng of Ft. (B). Nanocarriers with anti-ICAM antibodies binding to ICAM-negative or ICAM-positive REN cells; 1 μg of Ft. (C). Biodistribution of Ab/Ft and (Ab + SOD)/Ft nanoparticles *in vivo.* *$P < 0.05$ target-positive vs. target-negative cells. $^{\#}P < 0.05$ Ab vs. IgG.

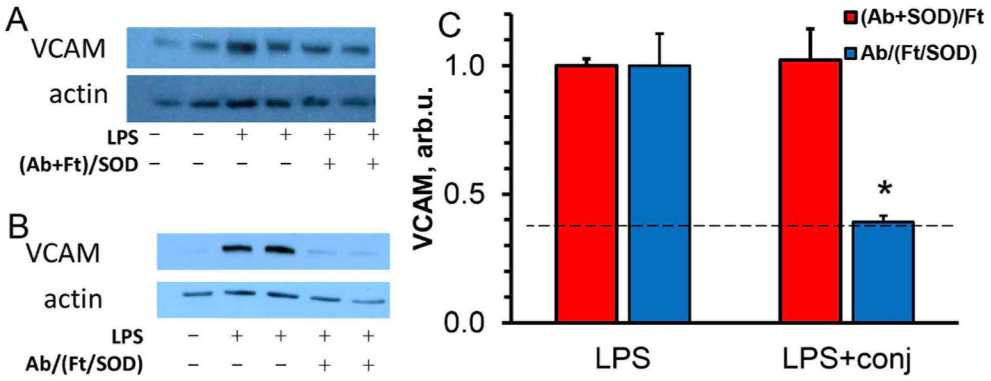

Fig. 12. ***In vivo*** **protection by antibody-ferritin-SOD nanoparticles against LPS-induced vascular lung inflammation.**

Comparison of ferritin particles with SOD loaded either outside or inside the particles (shown as (Ab + SOD)/Ft or Ab/(Ft/SOD), respectively). Animals were injected i.v. with the conjugates (75 μg SOD) 15 min prior to LPS (0.8 μg/kg). After 5 h the lungs were harvested, perfused with PBS, and homogenized. Lung VCAM expression was estimated by Western blotting (A and B, representative images for (Ab + SOD)/Ft and Ab/(Ft/SOD)) and quantified (C). $n \geq 3$; mean ± SD are shown; *$P < 0.05$ vs. LPS. Dashed line indicates VCAM level in naive animals.

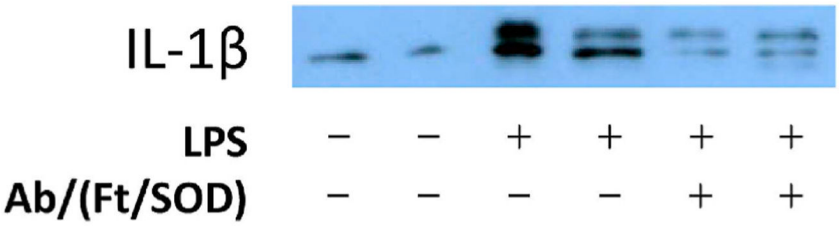

Fig. 13. Antibody-ferritin-SOD nanoparticles block LPS-induced systemic lung inflammation.
Ferritin particles with SOD loaded inside the particles, Ab/(Ft/SOD), were injected i.v. (75 μg SOD) 15 min prior to LPS (0.8 μg/kg). Lungs were harvested in 5 h, perfused with PBS, and homogenized. Lung pro-IL-1β expression was estimated by Western blotting.